

# Orbital Evolution of Satellite Galaxies in Self-Interacting Dark Matter Models

Fangzhou Jiang,<sup>1,2</sup> Manoj Kaplinghat,<sup>3</sup> Mariangela Lisanti,<sup>4</sup> and Oren Sloane<sup>4,5,\*</sup>

<sup>1</sup>*TAIR, California Institute of Technology, Pasadena, CA 91125, USA*

<sup>2</sup>*Carnegie Observatories, 813 Santa Barbara Street, Pasadena, CA 91101, USA*

<sup>3</sup>*University of Irvine, Irvine, CA 92697, USA*

<sup>4</sup>*Department of Physics, Princeton University, Princeton, NJ 08544, USA*

<sup>5</sup>*Center for Cosmology and Particle Physics, Department of Physics,*

*New York University, New York, NY 10003, USA*

(Dated: August 2, 2022)

Dark matter self interactions can leave distinctive signatures on the properties of satellite galaxies around Milky Way-like hosts through their impact on tidal stripping, ram pressure, and gravothermal collapse. We delineate the regions of self-interacting dark matter parameter space—specified by interaction cross section and a velocity scale—where each of these effects dominates, and show how the relative mass loss depends on the satellite’s initial mass, density profile and orbit. We obtain novel, conservative constraints in this parameter space using Milky Way satellite galaxies with notably high central densities and small pericenter distances. Our results for self-interacting dark matter models, in combination with constraints from clusters of galaxies, favor velocity-dependent cross sections that lead to gravothermal core collapse in the densest satellites.

**Introduction.**— Current observational efforts are characterizing the properties of satellite galaxies orbiting about the Milky Way [1, 2] and other Milky Way-like hosts in the Local Group [3, 4]. This wealth of new data provides an exciting opportunity to test the evolution of small-scale structure in Self-Interacting Dark Matter (SIDM) [5–15], as compared to Cold Dark Matter (CDM) [16–21]. SIDM arises generically in many theories [22], and is well-motivated from an astrophysical standpoint, as it potentially explains the diversity of galaxy rotation curves [23–26]. In this Letter, we present a first analysis of how velocity-dependent, anisotropic scattering between dark matter (DM) particles impacts the orbits of satellite galaxies.

For CDM, many ingredients affect a satellite’s orbit, including its initial mass, concentration, position and velocity. Satellites lose mass due to tidal forces of the host, especially near pericenter. Additionally, the more massive a satellite, the more dynamical friction it experiences, causing it to sink more deeply into the host’s potential. For SIDM, these effects continue to play a role. Furthermore, ram-pressure evaporation and deceleration, which arise from mass removal and momentum transfer following scattering events between DM particles in the satellite and host, impact the evolution [27].

The presence of a constant density core in SIDM satellites can increase the amount of mass that is tidally removed [7] as it orbits. This core is quasi-stable, however, and can undergo gravothermal collapse, which dramatically increases the central density of the satellite [12, 14, 28–33]. The core-collapse time scale depends on the satellite’s mass and concentration, mass loss along its orbit, and the velocity dependence of the cross section. Higher concentration satellites collapse faster,

with tidal stripping potentially accelerating the process further [11, 12, 33], and a sharply falling velocity dependence shortens the collapse time scale for lower-mass satellites [10]. Gravothermal collapse would increase the range of predicted DM densities in the Milky Way’s satellites, which may be necessary for SIDM to be consistent with the high inferred densities in ultra-faint satellite galaxies [10, 12, 34].

We perform a conceptual analysis using semi-analytical orbit integration to map the consequences of SIDM on satellite orbital evolution. In particular, the parameter space for which mass loss in SIDM is dominated by either tidal stripping or ram-pressure evaporation is identified. In the former case, the expected signature is an overall mass reduction in the satellite’s outer region over time, as compared to CDM. This behavior is most pronounced the more massive the satellite and the more eccentric its orbit. In the latter case, ram-pressure evaporation also efficiently removes mass from the central regions of the satellite, causing a lower central density than would be expected for CDM. We also map out regions where the effects of gravothermal collapse are expected to be important. These findings motivate new observational handles for testing SIDM.

We begin with an overview of how to model a satellite’s orbital evolution in CDM and SIDM. We then discuss the qualitative signatures of SIDM on satellite distributions around Milky Way-like hosts and identify regions of parameter space where important mass-loss effects dominate. Building on this understanding, we set novel, conservative SIDM constraints using the distributions and internal properties of Milky Way dwarf galaxies.

**Satellite Evolution.**— This study considers scenarios where DM particles of mass  $m_\chi$  interact via a light scalar or vector mediator of mass  $m_\phi$  with coupling  $\alpha_D$  [35–37]. In the non-relativistic limit, elastic self-scattering is well-described by a Yukawa potential, and

\* Corresponding author - oslane@princeton.edu / os2124@nyu.edu

when  $\alpha_D m_\chi / m_\phi \ll 2\pi$ , the cross section can be calculated using the Born approximation,

$$\frac{d\sigma}{d\theta} = \frac{\sigma_0 \sin \theta}{2 \left[ 1 + \frac{v^2}{\omega^2} \sin^2 \frac{\theta}{2} \right]^2}, \quad (1)$$

where  $\sigma_0 \equiv 4\pi\alpha_D^2 m_\chi^2 / m_\phi^4$ ,  $\omega \equiv m_\phi / m_\chi$ , and  $v$  is the velocity difference between the interacting particles (the notation  $\sigma_m$  or  $\sigma_{0m}$  will be used as shorthands for  $\sigma / m_\chi$  or  $\sigma_0 / m_\chi$  respectively). One benefit of using satellite systems to probe Eq. (1) is the separation of scales between the host and its satellites. Specifically, interactions within the satellite probe velocity scales of order the satellite's virial velocity,  $\mathcal{O}(10)$  km/s, while interactions between satellite and host particles probe velocities of order the virial velocity of the host,  $\mathcal{O}(100)$  km/s.

The three ingredients needed to properly model the evolution of infalling satellites for CDM and SIDM are:

(i) *Host & Satellite Density Profiles*.— Thermalization and heat flow resulting from self interactions can alter DM density profiles [38]. Any initially cuspy halo will exhibit inwards heat flow, resulting in a semi-stable isothermal configuration within the region where SIDM interactions are rapid enough. When baryons are unimportant, as is typically the case for satellites, the density profile develops a core at a radius  $r_c$  and transitions to a Navarro-Frenk-White (NFW) profile [39] beyond this point. For a Milky Way-like host, the presence of a baryonic disk leads to a cuspy profile that resembles an NFW profile with scale radius  $r_s$  [40, 41].

This semi-stable configuration does not remain intact indefinitely. Eventually, the direction of heat flow from self interactions changes, transferring heat outwards from the core. Because the core has negative specific heat, this results in a runaway gravothermal collapse process whereby the core heats up and shrinks simultaneously [28]. An important distinction should be made between the case when the SIDM Mean Free Path is either longer (LMFP) or shorter (SMFP) than the Jeans length of the core. In the LMFP regime, heat escapes efficiently from the core and the time scale for gravothermal collapse is given by  $t_{GC} \approx 290 / (\langle \sigma_m v \rangle \rho_{core})$ , where  $\rho_{core}$  is the core density [28]. In this phase, the density profile has a shrinking core radius,  $r_c$ . Outside  $r_c$ , the density decreases approximately as  $r^{-2.19}$  and transitions to the NFW profile when  $r \gtrsim r_s$  [28] for isolated halos. Note that gravothermal collapse in the LMFP regime cannot produce arbitrarily large densities at a given radius because the core shrinks while the density increases. Additionally, tidal stripping can significantly shorten  $t_{GC}$  by enhancing the rate of outwards heat flow for dense satellites [12, 32]. In the SMFP regime, heat gets trapped in the core and gravothermal collapse occurs much more rapidly.

(ii) *Mass loss*.— Mass loss during satellite infall occurs predominantly via tidal stripping and ram-pressure evaporation. The former is a result of gravitational tidal forces of the host that strip material from the satellite,

located at position  $r$ . These forces are efficient above the tidal radius,  $\ell_t$ , which is defined from the center of the satellite to be

$$\ell_t \approx r \left( \frac{m_{\text{sat}}(\ell_t)}{M_{\text{host}}(r)} \right)^{1/3}, \quad (2)$$

where  $m_{\text{sat}}(\ell)$  is the satellite's enclosed mass and  $M_{\text{host}}(r)$  is that of the host. The approximate mass-loss rate resulting from tidal stripping is

$$\dot{m}_{\text{TS}} \approx -\frac{m_{\text{sat}}(> \ell_t)}{t_{\text{dyn}}(r)}, \quad (3)$$

where  $m_{\text{sat}}(> \ell_t) \equiv m_{\text{sat}} - m_{\text{sat}}(\ell_t)$  and  $t_{\text{dyn}}(r)$  is the dynamical time [42]. The tidal radius has a strong dependence on the shape of the satellite's density profile. Comparing a cored SIDM to an NFW profile, one finds that when  $\ell_t \lesssim r_c$ , the tidal radius shrinks more rapidly for SIDM, resulting in more efficient tidal stripping compared to CDM.

Ram-pressure evaporation is the result of DM particle interactions between the satellite and the host. For any scattering event, if the final velocity of a particle is larger than the escape velocity of the satellite,  $v_{\text{esc}}$ , then the particle evaporates. The resulting mass-loss rate is

$$\dot{m}_{\text{RPe}} \approx -m_{\text{sat}} \eta_e \sigma_m v_{\text{sat}} \rho_{\text{host}}, \quad (4)$$

where  $v_{\text{sat}}$  is the satellite's velocity relative to the host,  $\rho_{\text{host}}$  is the DM density of the host at the satellite's position, and  $\eta_e$  is the evaporation fraction [27]. For cases of interest here, nearly all scattering events between host and satellite particles result in evaporation ( $\eta_e \approx 1$ ).

(iii) *Orbits*.— Assuming that the satellite is not significantly deformed by tidal forces and treating it as a point particle, the orbit is obtained by evaluating the equation of motion, which includes the acceleration due to dynamical friction [43] as well as ram-pressure deceleration. The latter arises from momentum transfer to the satellite from host-satellite scatterings, and is given by

$$\mathbf{a}_{\text{RPd}} \approx -\mathbf{v} \eta_d \sigma_m v_{\text{sat}} \rho_{\text{host}}, \quad (5)$$

where  $\eta_d$  is the deceleration fraction [27]. When  $v_{\text{sat}}$  is of order the virial velocity of the host, the deceleration fraction decreases rapidly with scaling  $\eta_d \propto (v_{\text{esc}}/v_{\text{sat}})^2$ . Thus, the work done by ram-pressure deceleration is only comparable to that done by dynamical friction for large  $\sigma_{0m}$  and  $\omega$  (see Fig. S1).

The orbital evolution of the satellite is obtained by numerically evaluating its equation of motion for any set of initial conditions. Full details on the semi-analytic orbit modeling are provided in Supplemental Material 1.

**Results.**— The left panel of Fig. 1 demonstrates how the mass of a  $10^{10} M_\odot$  satellite evolves with time for different assumptions of the DM model. The satellite is initialized at the virial radius of a  $10^{12} M_\odot$  host at  $z = 1$ , and two orbits are considered with pericenters at  $r_{\text{peri}} \approx 20$  and

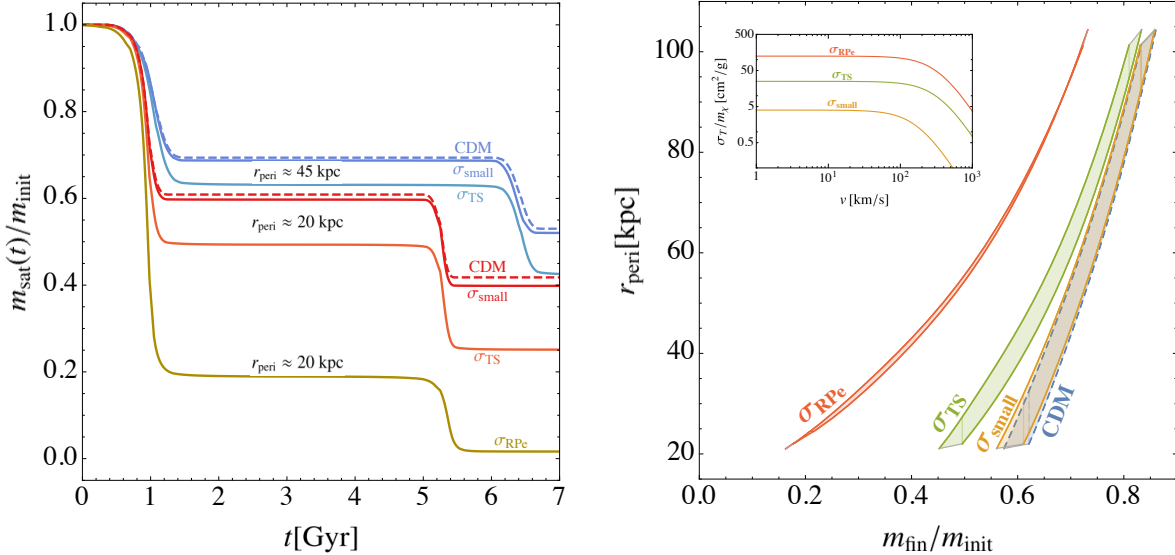


FIG. 1. Satellite evolution around a  $10^{12} M_{\odot}$  host. (Left) Time evolution of satellite mass, assuming  $m_{\text{init}} = 10^{10} M_{\odot}$ , for CDM (dashed) and SIDM (solid) for initially isothermal profiles. The SIDM parameters  $\{\sigma_{0m}, \omega\}$  correspond to:  $\sigma_{\text{small}} = \{4 \text{ cm}^2/\text{g}, 160 \text{ km/s}\}$ ,  $\sigma_{\text{TS}} = \{25 \text{ cm}^2/\text{g}, 315 \text{ km/s}\}$ , and  $\sigma_{\text{RPe}} = \{125 \text{ cm}^2/\text{g}, 315 \text{ km/s}\}$ . We contrast results for an eccentric orbit with pericenter  $r_{\text{peri}} \approx 20$  kpc with that of  $r_{\text{peri}} \approx 45$  kpc. Relative to CDM, SIDM results in increased mass loss, especially in the case of more radial orbits. (Right) Comparison of satellite mass loss in various scenarios. Initial satellite masses are considered in the range  $m_{\text{init}} \in [10^9, 10^{10.5}] M_{\odot}$  corresponding to the width of each band. Satellites are placed on orbits with varying pericenters and evolved for one pericentric passage. The ratio of final to initial mass is given on the horizontal axis; the four bands correspond to CDM,  $\sigma_{\text{small}}$ ,  $\sigma_{\text{TS}}$  and  $\sigma_{\text{RPe}}$ . The inset shows the velocity dependence of the transfer cross section for each SIDM scenario.

45 kpc (with the initial radius and velocity fixed to the virial radius and velocity of the host). The dashed curves show the results for CDM, while the solid curves show the results for three different sets of SIDM parameters, denoted as  $\sigma_{\text{small}}$ ,  $\sigma_{\text{TS}}$ , and  $\sigma_{\text{RPe}}$  (defined in the caption).  $\sigma_{\text{small}}$  gives results that are similar to CDM. For  $\sigma_{\text{TS}}$ , tidal stripping effects are more important for SIDM than for CDM. For  $\sigma_{\text{RPe}}$ , the ram-pressure evaporation rate strongly exceeds that of tidal stripping. Generally, satellite mass loss is more pronounced for SIDM than CDM, especially for larger interaction cross sections and more eccentric orbits.

The example of  $\sigma_{\text{RPe}}$  is particularly noteworthy. After its first pericentric passage,  $\sim 80\%$  of the satellite's mass is removed. The primary difference relative to  $\sigma_{\text{small}}$  and  $\sigma_{\text{TS}}$  is that mass loss due to ram-pressure evaporation dominates over tidal stripping, enhancing even further the difference between CDM and SIDM. While the latter preferentially removes mass from the outermost regions of the galaxy, the former has a more noticeable impact on its inner regions. This suggests that one can use the observation of a dwarf galaxy with low pericenter and high central density to constrain SIDM.

The right panel of Fig. 1 demonstrates in more detail how mass loss over one pericentric passage varies as a function of the SIDM parameters, the initial satellite mass,  $m_{\text{init}}$ , and the pericentric radius,  $r_{\text{peri}}$ . Such results can potentially be used to infer the microscopic

properties of DM from observations such as the distribution of satellites around their hosts. The four bands correspond to CDM (dashed) and the three example SIDM cross sections of the left panel (solid). From right to left across each band, the initial masses span  $m_{\text{init}} \in [10^9, 10^{10.5}] M_{\odot}$ . The results show that tidal stripping is more effective at creating differences between SIDM and CDM for larger mass satellites with smaller pericenters. The reason for this is two-fold. First, the more massive a satellite, the more dynamical friction it experiences causing its orbit to decay and its pericenter to decrease. This effect becomes even more pronounced after additional pericentric passages. Second, more massive satellites have larger values of  $r_c$ , which further enhance tidal stripping. For  $\sigma_{\text{RPe}}$ , a sizable difference is already observed for large pericenters. For small pericenters, the difference between SIDM and CDM is dramatic, with the SIDM satellite losing a large fraction of its mass.

Next, we build a conceptual map in SIDM parameter space showing where various mechanisms dominate a satellite's mass-loss evolution. In Fig. 2 (left), the colored areas demarcate the regions of interest for satellites with  $m_{\text{init}} \in [10^9, 10^{10}] M_{\odot}$  orbiting about a  $10^{12} M_{\odot}$  host. The orbital parameters are the same as the  $r_{\text{peri}} \approx 20$  kpc example in Fig. 1, and each satellite is evolved for 7 Gyr. The concentration of each satellite corresponds to the best-fit concentration-mass relation of Ref. [45] at  $z = 1$ . The comparison between SIDM and CDM is done by av-

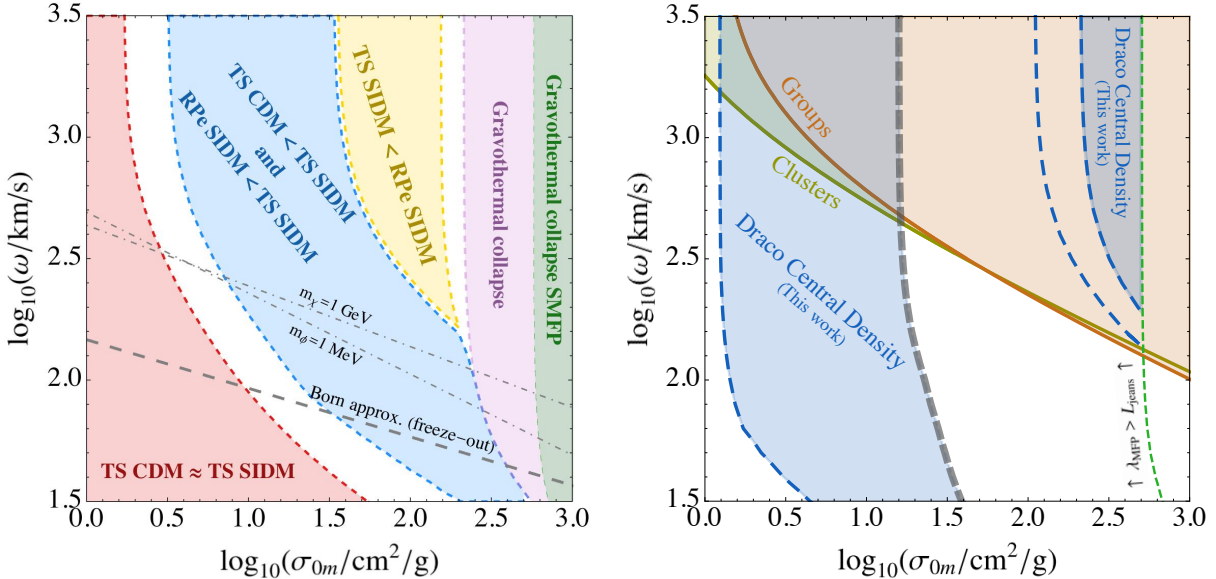


FIG. 2. (Left) A schematic diagram showing regions in SIDM parameter space where particular effects dominate in affecting a satellite's mass-loss evolution within the initial mass range  $m_{\text{init}} \in [10^9, 10^{10}] M_{\odot}$  and for the same orbital parameters as in the  $r_{\text{peri}} \approx 20$  kpc examples in Fig. 1. White regions indicate parameters where not all satellites in the mass range fall into a given category. In the red region, there is little observable difference in mass loss between CDM versus SIDM. In the blue region, tidal stripping (TS) is more effective in SIDM than in CDM, causing faster mass removal from the outskirts of SIDM satellites. In the yellow region, ram-pressure evaporation (RPe) dominates over tidal stripping for SIDM satellites, causing efficient mass removal from central regions. In the pink and green regions, gravothermal collapse becomes relevant either in the long or short mean free path regimes for isolated satellites; to the left of these regions, gravothermal collapse still plays a role as the collapse timescale can be reduced due to tidal stripping. Also shown in grey, are curves relevant for a dark sector populated by thermal freeze-out of  $\chi\chi \rightarrow \phi\phi$ . Above the dashed curve, the Born approximation holds for a scenario where  $\alpha_D$  is fixed to give the correct thermal abundance for dark matter. The dotted-dashed curves correspond to example values for  $m_{\chi}$  and  $m_{\phi}$ . (Right) Conservative constraints based on measurements of Draco's central density, which arise from over-coring of an isothermal SIDM profile (left-most dark-blue region) and excessive mass removal from ram-pressure evaporation (right-most dark-blue region), shown for the  $2\sigma$  lower limit on the measurement of  $\rho_{150}$  for Draco. Also shown are existing 95% confidence-level bounds from galaxy groups (brown) and clusters (yellow) [44].

eraging the mass loss over the last 2.5 Gyrs of the orbits.

In the red region, the ratio of mass loss between SIDM and CDM is less than 5% and little difference is expected in the satellite distribution. In the blue region, tidal stripping removes more mass for an SIDM satellite than for its CDM counterpart. Here, ram-pressure evaporation is small and therefore most mass is lost on the outskirts of the satellite. In the yellow region, ram-pressure evaporation in SIDM dominates over tidal stripping, and significant mass loss is expected from the centers of SIDM satellites. These results differ from those in Ref. [13], which found that satellites are preferentially destroyed in SIDM halos solely because of ram-pressure stripping. This is likely explained by the fact that Ref. [13] used DM-only simulations where the host was cored, thereby reducing the effects of tidal stripping.

The boundary of the blue region can be understood as follows. At the largest values of  $\omega$ , the cross section is velocity independent. As  $\omega$  decreases, velocity dependence becomes important. For small cross sections, the core is not at its maximal value and both the satellite's virial velocity and its velocity at pericenter (which is a few times

the virial velocity of the host) are important. At larger cross sections, the core is already maximal and only the virial velocity of the host sets the velocity behavior.

The pink region is where the gravothermal collapse timescale for an isolated halo is short,  $t_{\text{GC}} < 10$  Gyrs. The green region within the pink denotes parameters for which the MFP is shorter than the Jeans length of the core and collapse occurs in the more rapid SMFP regime. In both, tidal stripping and ram-pressure evaporation remain active, but calculating their effects requires accounting for the initially collapsed halo. A caveat to this is that even to the left of the pink region, where  $t_{\text{GC}}$  for an isolated halo is long, tidal stripping can significantly decrease its value. Therefore, the pink region should be thought of as the parameters where LMFP gravothermal collapse can occur for isolated satellites, either before infall or with large pericenters.

A clear understanding of the orbital effects that dominate for different  $\sigma_{0m}$  and  $\omega$  is critical for testing SIDM. We provide a proof-of-concept example of how to perform such tests, focusing on the Draco dwarf galaxy. Further details of this procedure are provided in Supplemental

Material 2. The first bound arises from the requirement that heating of the isothermal core not reduce Draco’s present-day central density,  $\rho_{150}$ , (at 150 pc) more than  $2\sigma$  below its measured value [11]. To obtain a conservative estimate of this bound, we marginalize over the unknown present-day mass of Draco by choosing the value that gives the largest central density at every point in parameter space. We also take the  $2\sigma$  upper limit for Draco’s concentration at  $z = 1$ . Finally, we require that  $t_{\text{GC}}$  is too long for gravothermal collapse to be active, even when tidal stripping effects are included. The resulting constraint corresponds to the left-most dark-blue region in Fig. 2 (right). In the limit of constant interaction cross section, these results are consistent with those of Ref. [8], albeit slightly weaker due to the conservative assumptions made here. A careful understanding of the role of gravothermal collapse in this region of parameter space enables us to extend the Draco bounds to lower velocity scales compared to Ref. [8].

The second bound arises in regimes where ram-pressure evaporation removes too much mass from the central regions of Draco during its most recent pericentric passage. To conservatively estimate this bound, Draco’s orbit is found by utilizing its measured current position and velocity [46] and assuming an initially fully gravothermally collapsed halo. We conservatively choose a core radius that gives the maximal possible density at 150 pc, where Draco’s density is measured. The resulting constraint corresponds to the right-most dark-blue region in Fig. 2 (right). The inner (outer) dashed curves correspond to the  $1\sigma$  lower (upper) limit on the Milky Way mass,  $M_{\text{MW}} = (1.3 \pm 0.3) \times 10^{12} M_{\odot}$  [47]. We only evolve the satellite for one orbital period; allowing for two full orbits results in bounds that closely track the outer dashed curve. It is likely that a full analysis will result in more of the high  $\omega$ , high  $\sigma_{0m}$  region being ruled out because ram-pressure evaporation destroys satellites, but our analysis also reveals that core collapse can insulate against that possibility.

The conservative bounds presented in this study identify regions of SIDM parameter space where a dedicated analysis of all known Milky Way dwarfs should have excellent sensitivity. Indeed, we have derived bounds using Ursa Minor, Segue 1, and Tucana 2, and they turn out to be similar (see Fig. S2). Fig. 2 (right) also shows bounds from groups and clusters [44], which are more stringent than the Bullet Cluster bounds [48]. For clusters, there are comparable bounds from oscillations of brightest cluster galaxies [49] and a tighter bound from a dedicated strong lensing analysis [50]. Combined with the cluster and group bounds, our results favor velocity-dependent SIDM cross sections that can trigger core collapse.

**Conclusions.**— This Letter provides both a quantitative and intuitive understanding of the relevant SIDM physics that affects the internal properties of satellites, as well as their distributions within a Milky Way-like host. The orbits of satellites with given initial mass,

concentration, and eccentricity were computed for different anisotropic, velocity-dependent cross sections and compared. This semi-analytical approach is beneficial for identifying the physical mechanisms that affect the satellite’s orbit in different regions of SIDM parameter space, and should hold so long as the satellite is not significantly tidally deformed along its orbit.

We identified several key regimes of interest in SIDM parameter space where particular mechanisms affect satellite orbits. Additionally, we placed conservative constraints on SIDM parameter space using the measured central densities of Draco, Ursa Minor, Segue 1 and Tucana 2, which all provided consistent results. When combined with group and cluster constraints, our findings strongly argue for SIDM models where velocity-dependent interactions can trigger gravothermal core collapse in at least some of the satellites.

The results of this work underscore how individual Milky Way satellites can provide remarkable sensitivity to velocity-dependent DM self interactions. We also anticipate that the mass-loss and gravothermal collapse mechanisms studied here may translate into potentially observable differences in the population statistics of satellites. With the abundance of observational data rapidly becoming available for both the Milky Way and other Milky Way-like systems in the Local Group, satellite galaxies will provide a critical—and potentially definitive—exploration of the SIDM parameter space.

**Acknowledgements.**— The authors gratefully acknowledge S. Carlsten, J. Greene, E. Nadler, and P. Natarajan for useful conversations. FJ is supported by the Troesh Scholarship at Caltech. MK is supported by the NSF under Award Number 1915005. ML and OS are supported by the DOE under Award Number DE-SC0007968 and the Binational Science Foundation (grant No. 2018140). ML is also supported by the Cottrell Scholar Program through the Research Corporation for Science Advancement.

- [1] A. W. McConnachie, *Astron. J.* **144**, 4 (2012), 1204.1562.
- [2] T. K. Fritz, G. Battaglia, M. S. Pawlowski, N. Kallivayalil, R. van der Marel, S. T. Sohn, C. Brook, and G. Besla, *Astron. Astrophys.* **619**, A103 (2018), 1805.00908.
- [3] S. G. Carlsten, J. E. Greene, A. H. G. Peter, J. P. Greco, and R. L. Beaton, *Astrophys. J.* **902**, 124 (2020), 2006.02444.
- [4] Y.-Y. Mao, M. Geha, R. H. Wechsler, B. Weiner, E. J. Tollerud, E. O. Nadler, and N. Kallivayalil, *Astrophys. J.* **907**, 85 (2021), 2008.12783.
- [5] M. Vogelsberger, J. Zavala, and A. Loeb, *Mon. Not. Roy. Astron. Soc.* **423**, 3740 (2012), 1201.5892.
- [6] J. Zavala, M. Vogelsberger, and M. G. Walker, *Mon. Not. Roy. Astron. Soc.* **431**, L20 (2013), 1211.6426.
- [7] G. A. Dooley, A. H. G. Peter, M. Vogelsberger, J. Zavala, and A. Frebel, *Mon. Not. Roy. Astron. Soc.* **461**, 710 (2016), 1603.08919.

[8] J. I. Read, M. G. Walker, and P. Steger, *Mon. Not. Roy. Astron. Soc.* **481**, 860 (2018), 1805.06934.

[9] V. H. Robles, T. Kelley, J. S. Bullock, and M. Kaplinghat, *Mon. Not. Roy. Astron. Soc.* **490**, 2117 (2019), 1903.01469.

[10] J. Zavala, M. R. Lovell, M. Vogelsberger, and J. D. Burger, *Phys. Rev. D* **100**, 063007 (2019), 1904.09998.

[11] M. Kaplinghat, M. Valli, and H.-B. Yu, *Mon. Not. Roy. Astron. Soc.* **490**, 231 (2019), 1904.04939.

[12] F. Kahlhoefer, M. Kaplinghat, T. R. Slatyer, and C.-L. Wu, *JCAP* **12**, 010 (2019), 1904.10539.

[13] E. O. Nadler, A. Banerjee, S. Adhikari, Y.-Y. Mao, and R. H. Wechsler, *Astrophys. J.* **896**, 112 (2020), 2001.08754.

[14] H. C. Turner, M. R. Lovell, J. Zavala, and M. Vogelsberger (2020), 2010.02924.

[15] C. A. Correa, *Mon. Not. Roy. Astron. Soc.* **503**, 920 (2021), 2007.02958.

[16] A. V. Kravtsov, O. Y. Gnedin, and A. A. Klypin, *Astroph. J.* **609**, 482 (2004), astro-ph/0401088.

[17] E. D’Onghia, V. Springel, L. Hernquist, and D. Keres, *Astroph. J.* **709**, 1138 (2010), 0907.3482.

[18] J. Peñarrubia, A. J. Benson, M. G. Walker, G. Gilmore, A. W. McConnachie, and L. Mayer, *Mon. Not. Roy. Astron. Soc.* **406**, 1290 (2010), 1002.3376.

[19] G. A. Dooley, A. H. G. Peter, T. Yang, B. Willman, B. F. Griffen, and A. Frebel, *Mon. Not. Roy. Astron. Soc.* **471**, 4894 (2017), 1610.00708.

[20] S. Garrison-Kimmel, A. Wetzel, J. S. Bullock, P. F. Hopkins, M. Boylan-Kolchin, C.-A. Faucher-Giguère, D. Kereš, E. Quataert, R. E. Sanderson, A. S. Graus, et al., *Mon. Not. Roy. Astron. Soc.* **471**, 1709 (2017), 1701.03792.

[21] J. Samuel, A. Wetzel, E. Tollerud, S. Garrison-Kimmel, S. Loebman, K. El-Badry, P. F. Hopkins, M. Boylan-Kolchin, C.-A. Faucher-Giguère, J. S. Bullock, et al., *Mon. Not. Roy. Astron. Soc.* **491**, 1471 (2020), 1904.11508.

[22] S. Tulin and H.-B. Yu, *Phys. Rept.* **730**, 1 (2018), 1705.02358.

[23] A. Kamada, M. Kaplinghat, A. B. Pace, and H.-B. Yu, *Phys. Rev. Lett.* **119**, 111102 (2017), 1611.02716.

[24] P. Creasey, O. Sameie, L. V. Sales, H.-B. Yu, M. Vogelsberger, and J. Zavala, *Mon. Not. Roy. Astron. Soc.* **468**, 2283 (2017), 1612.03903.

[25] T. Ren, A. Kwa, M. Kaplinghat, and H.-B. Yu, *Phys. Rev. X* **9**, 031020 (2019), 1808.05695.

[26] M. Kaplinghat, T. Ren, and H.-B. Yu, *JCAP* **06**, 027 (2020), 1911.00544.

[27] J. Kummer, F. Kahlhoefer, and K. Schmidt-Hoberg, *Mon. Not. Roy. Astron. Soc.* **474**, 388 (2018), 1706.04794.

[28] S. Balberg, S. L. Shapiro, and S. Inagaki, *Astrophys. J.* **568**, 475 (2002), astro-ph/0110561.

[29] J. Koda and P. R. Shapiro, *Mon. Not. Roy. Astron. Soc.* **415**, 1125 (2011), 1101.3097.

[30] O. D. Elbert, J. S. Bullock, S. Garrison-Kimmel, M. Rocha, J. Oñorbe, and A. H. G. Peter, *Mon. Not. Roy. Astron. Soc.* **453**, 29 (2015), 1412.1477.

[31] R. Essig, S. D. McDermott, H.-B. Yu, and Y.-M. Zhong, *Phys. Rev. Lett.* **123**, 121102 (2019), 1809.01144.

[32] H. Nishikawa, K. K. Boddy, and M. Kaplinghat, *Phys. Rev. D* **101**, 063009 (2020), 1901.00499.

[33] O. Sameie, H.-B. Yu, L. V. Sales, M. Vogelsberger, and J. Zavala, *Phys. Rev. Lett.* **124**, 141102 (2020), 1904.07872.

[34] S. Y. Kim and A. H. G. Peter (2021), 2106.09050.

[35] J. L. Feng, M. Kaplinghat, H. Tu, and H.-B. Yu, *JCAP* **07**, 004 (2009), 0905.3039.

[36] A. Loeb and N. Weiner, *Phys. Rev. Lett.* **106**, 171302 (2011), 1011.6374.

[37] M. Kaplinghat, S. Tulin, and H.-B. Yu, *Phys. Rev. Lett.* **116**, 041302 (2016), 1508.03339.

[38] D. N. Spergel and P. J. Steinhardt, *Phys. Rev. Lett.* **84**, 3760 (2000), astro-ph/9909386.

[39] J. F. Navarro, C. S. Frenk, and S. D. M. White, *Astrophys. J.* **490**, 493 (1997), astro-ph/9611107.

[40] M. Kaplinghat, R. E. Keeley, T. Linden, and H.-B. Yu, *Phys. Rev. Lett.* **113**, 021302 (2014), 1311.6524.

[41] O. Sameie, P. Creasey, H.-B. Yu, L. V. Sales, M. Vogelsberger, and J. Zavala, *Mon. Not. Roy. Astron. Soc.* **479**, 359 (2018), 1801.09682.

[42] F. Jiang, A. Dekel, J. Freundlich, F. C. van den Bosch, S. B. Green, P. F. Hopkins, A. Benson, and X. Du, *Mon. Not. Roy. Astron. Soc.* **502**, 621 (2021), 2005.05974.

[43] S. Chandrasekhar, *Astrophys. J.* **97**, 255 (1943).

[44] L. Sagunski, S. Gad-Nasr, B. Colquhoun, A. Robertson, and S. Tulin, *JCAP* **01**, 024 (2021), 2006.12515.

[45] A. A. Dutton and A. V. Macciò, *Mon. Not. Roy. Astron. Soc.* **441**, 3359 (2014), 1402.7073.

[46] E. Patel, N. Kallivayalil, N. Garavito-Camargo, G. Besla, D. R. Weisz, R. P. van der Marel, M. Boylan-Kolchin, M. S. Pawlowski, and F. A. Gómez, *Astrophys. J.* **893**, 121 (2020).

[47] J. Bland-Hawthorn and O. Gerhard, *Annual Review of Astronomy and Astrophysics* **54**, 529 (2016).

[48] S. W. Randall, M. Markevitch, D. Clowe, A. H. Gonzalez, and M. Bradac, *Astrophys. J.* **679**, 1173 (2008), 0704.0261.

[49] D. Harvey, A. Robertson, R. Massey, and I. G. McCarthy, *Mon. Not. Roy. Astron. Soc.* **488**, 1572 (2019), 1812.06981.

[50] K. E. Andrade, J. Fuson, S. Gad-Nasr, D. Kong, Q. Minor, M. G. Roberts, and M. Kaplinghat (2020), 2012.06611.

[51] Z.-Z. Li, Y.-Z. Qian, J. Han, T. S. Li, W. Wang, and Y. P. Jing, *Astrophys. J.* **894**, 10 (2020).

[52] S. Tulin, H.-B. Yu, and K. M. Zurek, *Phys. Rev. D* **87**, 115007 (2013), 1302.3898.

[53] A. Robertson, R. Massey, and V. Eke, *Mon. Not. Roy. Astron. Soc.* **467**, 4719 (2017), 1612.03906.

[54] A. Robertson, D. Harvey, R. Massey, V. Eke, I. G. McCarthy, M. Jauzac, B. Li, and J. Schaye, *Mon. Not. Roy. Astron. Soc.* **488**, 3646 (2019), 1810.05649.

[55] S. B. Green, F. C. van den Bosch, and F. Jiang, *Mon. Not. Roy. Astron. Soc.* **503**, 4075 (2021), ISSN 0035-8711, 2103.01227.

[56] S. von Hoerner, *Astrophys. J.* **125**, 451 (1957).

[57] I. King, *Astron. J.* **67**, 471 (1962).

[58] G. D. Martinez, Q. E. Minor, J. Bullock, M. Kaplinghat, J. D. Simon, and M. Geha, *Astrophys. J.* **738**, 55 (2011), 1008.4585.

[59] M. G. Walker, M. Mateo, E. W. Olszewski, S. Koposov, V. Belokurov, P. Jethwa, D. L. Nidever, V. Bonnivard, J. I. B. III, E. F. Bell, et al., *Astrophys. J.* **819**, 53 (2016).

[60] J. I. Read and D. Erkal, *Mon. Not. Roy. Astron. Soc.* **487**, 5799 (2019), 1807.07093.

[61] R. J. J. Grand, F. Marinacci, R. Pakmor, C. M. Simpson, A. J. Kelly, F. A. Gómez, A. Jenkins, V. Springel, C. S.

Frenk, and S. D. M. White (2021), 2105.04560.

[62] S. P. Fillingham, M. C. Cooper, T. Kelley, M. K. Rodriguez Wimberly, M. Boylan-Kolchin, J. S. Bullock, S. Garrison-Kimmel, M. S. Pawlowski, and C. Wheeler (2019), 1906.04180.

[63] R. D'Souza and E. F. Bell, *Mon. Not. Roy. Astron. Soc.* **504**, 5270 (2021), 2104.13249.

[64] J. D. Simon, *Astrophys. J.* **863**, 89 (2018).

[65] J. E. Taylor and J. F. Navarro, *Astrophys. J.* **563**, 483 (2001), astro-ph/0104002.

[66] M. Rocha, A. H. G. Peter, J. S. Bullock, M. Kaplinghat, S. Garrison-Kimmel, J. Onorbe, and L. A. Moustakas, *Mon. Not. Roy. Astron. Soc.* **430**, 81 (2013), 1208.3025.

[67] Y. Ascasibar and S. Gottlöber, *Mon. Not. Roy. Astron. Soc.* **386**, 2022 (2008), 0802.4348.

# Orbital Evolution of Satellite Galaxies in Self-Interacting Dark Matter Models

## Supplemental Material

Fangzhou Jiang, Manoj Kaplinghat, Mariangela Lisanti, and Oren Sloane

The first section of the Supplemental Material provides a detailed description of the procedure used in this study to evolve the orbits of SIDM and CDM satellites. The second section of the Supplemental Material describes the analysis performed to obtain the Draco bounds in the right panel of Fig. 2; conservative constraints for three additional dwarf galaxies are also presented.

### 1. Detailed Procedure for Satellite Orbit Modeling

As discussed in the main Letter, there are three key ingredients required to model a satellite's orbit in both the CDM and SIDM cases. This Supplemental Material explores these ingredients in detail, focusing on: (a) the density profiles of the satellite and host halos, (b) the formalism for describing satellite mass loss from tidal stripping and ram-pressure evaporation, and (c) the numerical method for solving the equation of motion of the satellite.

#### a. Host & Satellite Density Profiles

The density profile for a CDM satellite or host, as well as for a baryon-dominated SIDM host, is taken to be an NFW profile [39]. The enclosed mass of this profile has the form

$$M_{\text{NFW}}(r) = 4\pi\rho_0 r_s^3 \left[ \ln\left(\frac{r+r_s}{r_s}\right) - \frac{r}{r+r_s} \right], \quad (\text{S1})$$

where  $r_s$  is the scale radius and  $\rho_0$  is a normalization density. SIDM satellite profiles that are not gravothermally collapsed are modeled as

$$M_{\text{SIDM}}(r) = M_{\text{NFW}}(r) \cdot \tanh\left(\frac{r}{r_c}\right), \quad (\text{S2})$$

where the core radius is defined as  $r_c = \min[0.5r_1, r_s]$  with  $r_1$  the radius below which interactions occur at least once within the age of the halo (see below). This form of the enclosed mass has an analytical solution for the density profile and also has the same total enclosed mass at  $r \gg r_c$  as that of an NFW profile with the same  $\rho_0$  and  $r_s$ . The density distributions corresponding to Eqs. (S1) and (S2) can be found by differentiating the formula for the enclosed mass, and are initially truncated at the virial radius. For this profile, the core density is  $3/2 \times \rho_0 r_s / r_c$ .

Once the virial mass,  $M_{200}$ , of the halo is specified, its virial radius is determined by requiring that the average halo density is 200 times the critical density,  $\rho_{\text{crit}}(z)$ . The NFW scale radius then follows from the concentration-mass relation in Ref. [45], with  $\rho_0$  obtained by requiring that the enclosed mass at  $r_{200}$  gives  $M_{200}$ . Unless otherwise specified, the concentration of the satellite galaxy is evaluated at redshift  $z = 1$ , corresponding to the time of infall in our examples. Note that, for the host halo specifically, we take a concentration of  $c_{200} = 10$  and assume a total mass of  $10^{12} M_\odot$  at time of satellite infall, unless otherwise specified. For the case of an NFW profile, this procedure is all that is required to set the free parameters of the halo model. For the SIDM profile, this procedure sets the properties of the NFW profile before self interactions heat the central regions of the halo and the core forms. During this process, some DM will be pushed out from the innermost region of the halo. We have verified using idealized  $N$ -body SIDM simulations and cosmological FIRE-SIDM simulations [51] that the original NFW profile provides a good description beyond  $r_c$ .

The value of the radius  $r_1$  is approximated using the following equation:

$$\langle \sigma_m v \rangle \rho_{\text{SIDM}}(r_1) t_{\text{age}} = 1, \quad (\text{S3})$$

where  $t_{\text{age}}$  is the age of the satellite. The velocity-averaged transfer cross section  $\langle \sigma_m v \rangle$  is given by,

$$\langle \sigma_m v \rangle = \frac{1}{m_\chi} \int f(\mathbf{v}_1) f(\mathbf{v}_2) v \frac{d\sigma}{d\theta} (1 - \cos \theta) d^3 \mathbf{v}_1 d^3 \mathbf{v}_2 d\theta, \quad (\text{S4})$$

where  $\mathbf{v} \equiv \mathbf{v}_1 - \mathbf{v}_2$  is the relative velocity, and  $\theta$  is the scattering angle. This can be simplified to a single integral over  $v$ . Note that the  $1 - \cos \theta$  weighting does not suppress contributions from scattering events where the two particles

exchange velocities ( $\theta \simeq \pi$ ), which would not change the halo density profile. To take this into account, other weights such as  $\sin^2 \theta$  (viscosity cross section) [52] or  $(1 - |\cos \theta|)$  [53, 54] have been proposed. The  $(1 - |\cos \theta|)$  weighted cross section is about a factor of 2 smaller for  $w$  larger than the dispersion of DM, while for small  $w$  the differences are 20-30%. The  $\sin^2 \theta$  weighted cross section is different from the  $1 - \cos(\theta)$  by 33% or lesser, depending on the value of  $w$ . This  $\mathcal{O}(1)$  systematic, which should be kept in mind when interpreting our results, should be resolved in the future with more simulations covering a range of  $w$  values.

In the equation above,  $f(\mathbf{v})$  is the Maxwell-Boltzmann velocity distribution for the DM,

$$f(\mathbf{v}) = \left( \frac{3}{2\pi\sigma_v^2} \right)^{3/2} e^{-3\mathbf{v}^2/2\sigma_v^2} \quad (\text{S5})$$

and  $\sigma_v$  is the root-mean-square velocity dispersion. Assuming an isotropic velocity distribution, then  $\sigma_v^2 = 3\sigma_r^2$ , where the radial dispersion  $\sigma_r$  follows from the radial Jeans equation,

$$\sigma_r^2(r) = \frac{1}{\rho_{\text{SIDM}}(r)} \int_r^\infty \frac{\rho_{\text{SIDM}}(r') v^2(r')}{r'} dr', \quad (\text{S6})$$

with  $v^2(r) = GM_{\text{SIDM}}(r)/r$ . With  $r_1$  obtained in the way detailed above, we find that using  $r_c = 0.5r_1$  in Eq. (S2) provides an accurate fit to the SIDM profile obtained from isothermal Jeans modeling or from idealized SIDM  $N$ -body simulations. For cross sections of  $\sigma_m = 1\text{--}20 \text{ cm}^2/\text{g}$  and for  $t_{\text{age}} = 1\text{--}10 \text{ Gyr}$ , Eq. (S2) with  $r_c = 0.5r_1$  agrees with simulation results to percent level. For larger cross sections that yield  $r_1 > r_s$ , we find that setting  $r_c = r_s$  provides better fits.

For certain ranges of parameter space, gravothermal collapse can affect the density distribution of SIDM halos and Eq. (S2) no longer suffices. Gravothermally collapsed profiles in the LMFP regime are modeled based on the results of numerically solving for the self-similar solution in Ref. [28]. In this regime, the solution for the gravothermally collapsing region and its surroundings takes the form of a flat core within a shrinking radius,  $r_c$ . Above this radius, the density decreases as  $\rho_{\text{GC}} \propto r^{-2.19}$  before transitioning to  $\rho_{\text{NFW}}(r)$  above the radius  $r \gtrsim r_{\text{GC}}$ . To model the scenario of a halo that initially thermalizes and cores below  $r_c$  and eventually undergoes collapse, we use a phenomenological profile of the form

$$\rho_{\text{GC}}(r) = \frac{\rho_0}{(r/r_{\text{GC}})^\alpha (1 + r/r_{\text{GC}})^{3-\alpha}} \tanh \left( \frac{r}{\min[r_c, r_{\text{GC}}]} \right)^\alpha, \quad (\text{S7})$$

where  $\alpha = 2.19$  and  $r_{\text{GC}} = 2r_s$ . This profile decreases as  $r^{-3}$  when  $r \gg r_{\text{GC}}$ , as  $r^{-2.19}$  when  $r_c < r < r_{\text{GC}}$  and flattens out when  $r < r_c$ , as would be expected from a collapsing core in the LMFP regime. We have verified that this density model is qualitatively similar to what was found in SIDM simulations with collapsing halos [32, 33]. Note, however, that Ref. [14] finds a steeper single power-law profile in the region outside the core of  $r^{-3}$  for satellites deep in the core-collapse phase. Such a change to the profile would mildly effect the ram-pressure bounds in Fig. 2 (right) and Fig. S2.

### b. Mass Loss

Satellite mass is lost in one of two ways. For both SIDM and CDM scenarios, tidal stripping can remove mass from the outskirts of the satellite. The tidal stripping mass-loss rate is given by Eq. (3), but with the addition of the  $\mathcal{O}(1)$  constant  $\mathcal{A} = 0.55$  [55],

$$\dot{m}_{\text{TS}} \approx -\mathcal{A} \frac{m_{\text{sat}}(> \ell_t)}{t_{\text{dyn}}(r)}. \quad (\text{S8})$$

The tidal radius,  $\ell_t$ , is calculated with Eq. (2), but modified to include the effects of both the tidal force and centrifugal force acting on the satellite [56, 57],

$$\ell_t \simeq r \left[ \frac{m_{\text{sat}}(\ell_t)/M_{\text{host}}(r)}{2 - \frac{d \ln M_{\text{host}}}{d \ln r} + \frac{v_{\text{tan}}^2(r)}{v_{\text{circ}}^2(r)}} \right]^{1/3}, \quad (\text{S9})$$

where  $v_{\text{tan}}(r) = |\hat{r} \times \mathbf{v}_{\text{sat}}|$  is the instantaneous tangential velocity of the satellite and  $v_{\text{circ}}(r) = \sqrt{GM_{\text{host}}(r)/r^2}$  is its circular velocity. The dynamical time is taken to be

$$t_{\text{dyn}}(r) = \sqrt{\frac{3\pi}{16G\bar{\rho}_{\text{host}}(r)}}, \quad (\text{S10})$$

where  $\bar{\rho}_{\text{host}}$  is the average density of the host within radius  $r$  [42].

For SIDM satellites only, ram-pressure evaporation can remove mass from all regions of the satellite. Ram-pressure evaporation is calculated according to Eq. (4), with the evaporation fraction given by

$$\eta_e = \frac{1}{\sigma} \int_{\pi - \theta_{\text{crit}}}^{\theta_{\text{crit}}} \frac{d\sigma}{d\theta} d\theta \quad , \text{ where } \theta_{\text{crit}} = \arccos \left( \frac{x^2 - 1}{x^2 + 1} \right) \quad (\text{S11})$$

and  $x = \bar{v}_{\text{esc}}/v_{\text{sat}}$  with  $\bar{v}_{\text{esc}}$  the average escape velocity of the satellite. The cross section,  $\sigma_m$ , in Eq. (4) is evaluated at a velocity equal to the satellite's velocity with respect to the host plus the average escape velocity of the satellite,  $v = v_{\text{sat}} + \bar{v}_{\text{esc}}$  [27]. The latter is a reasonable approximation because host-satellite scattering events typically occur close to the center of the satellite. In general,  $\bar{v}_{\text{esc}}/v_{\text{sat}} \ll 1$  for the cases of interest here, so this approximation is sufficient even for scatterings that occur in the outer regions of the satellite.

Knowing both the mass-loss rate from tidal stripping and ram-pressure evaporation through Eqs. (3) and (4), a prescription can be established to track the total mass and density profile of the satellite along its orbit. For any small time step,  $\Delta t = t' - t$ , the tidal stripping or ram-pressure evaporation mass loss can be evaluated by

$$\Delta m_{\text{TS/RPe}} = \int_t^{t'} \dot{m}_{\text{TS/RPe}} dt, \quad (\text{S12})$$

where  $\Delta m_{\text{TS/RPe}}$  are typically negative.

Any mass that is removed via tidal stripping is taken away from the outer-most region of the satellite halo. This is modeled by defining a truncation radius that evolves over time. At a given time step, the truncation radius is taken to decrease from  $r_{\text{trunc}}$  to  $r'_{\text{trunc}}$  such that the mass enclosed between these radii is equal to  $\Delta m_{\text{TS}}$ , namely,

$$M(\rho_0, r'_{\text{trunc}}) - M(\rho_0, r_{\text{trunc}}) = \Delta m_{\text{TS}}. \quad (\text{S13})$$

In contrast, mass that is removed via ram-pressure evaporation is taken from all regions of the satellite by changing the normalization of its density profile. This prescription removes mass from regions of the halo in a fashion that is linearly proportional to the local density at any given point. The normalization is taken to change from  $\rho_0$  to  $\rho'_0$  such that the mass difference is equal to  $\Delta m_{\text{RPe}}$ , namely,

$$M(\rho'_0, r_{\text{trunc}}) - M(\rho_0, r_{\text{trunc}}) = \Delta m_{\text{RPe}}. \quad (\text{S14})$$

If the velocity of the satellite is anomalously small, then  $\Delta m_{\text{RPe}}$  can be positive, i.e., the satellite accretes mass. Although this is possible, it is never the case for the scenarios considered in this study.

### c. Orbits

The evolution of the satellite's orbit is obtained by solving the following equation of motion:

$$\mathbf{a}_{\text{tot}} = -\nabla\Phi + \mathbf{a}_{\text{DF}} + \mathbf{a}_{\text{RPe}}, \quad (\text{S15})$$

where  $\Phi$  is the gravitational potential of the host,  $\mathbf{a}_{\text{DF}}$  is the acceleration due to dynamical friction, and  $\mathbf{a}_{\text{RPe}}$  is the ram-pressure deceleration. The dynamical friction is modeled using the Chandrasekhar formula [43],

$$\mathbf{a}_{\text{DF}} = -4\pi G^2 m_{\text{sat}} \rho_{\text{host}} \ln \Lambda F_{\text{v}}(v_{\text{sat}}) \frac{\mathbf{v}_{\text{sat}}}{v_{\text{sat}}^3}, \quad (\text{S16})$$

where the Coulomb logarithm is defined as  $\ln \Lambda = \min[s, 1] \ln(M_{\text{host}}/m_{\text{sat}})$  with  $s = (3r + r_{s,\text{host}})/(r + r_{s,\text{host}})$  and  $r_{s,\text{host}}$  the scale radius of the host [42]. Assuming an isotropic and Maxwellian host halo, then  $F_{\text{v}}(v_{\text{sat}}) = \text{Erf}(y) - 2ye^{-y^2}/\sqrt{\pi}$  with  $y = v_{\text{sat}}/(\sqrt{2}\sigma_{\text{r}})$ , where  $\sigma_{\text{r}}$  is the radial velocity dispersion of the host.

Ram-pressure deceleration, calculated according to Eq. (5), can affect a satellite's orbit, especially in regions of large self-interaction cross sections. For  $v_{\text{sat}} \gg v_{\text{esc}}$ , the deceleration fraction,  $\eta_d$ , is

$$\eta_d = \frac{1}{m_{\chi} v \sigma} \int \Delta p_z \frac{d\sigma}{d\theta} d\theta \approx \frac{1}{2} \left( \frac{v_{\text{esc}}}{v_{\text{sat}}} \right)^2, \quad (\text{S17})$$

where  $\Delta p_z$  is the change in momentum along the direction of motion of the incoming particles. The velocity dispersion,  $v_{\text{disp}}$ , of interacting particles causes a further suppression of  $\eta_d$  when  $v_{\text{sat}} \lesssim v_{\text{disp}}$ . However, at pericenter (when the

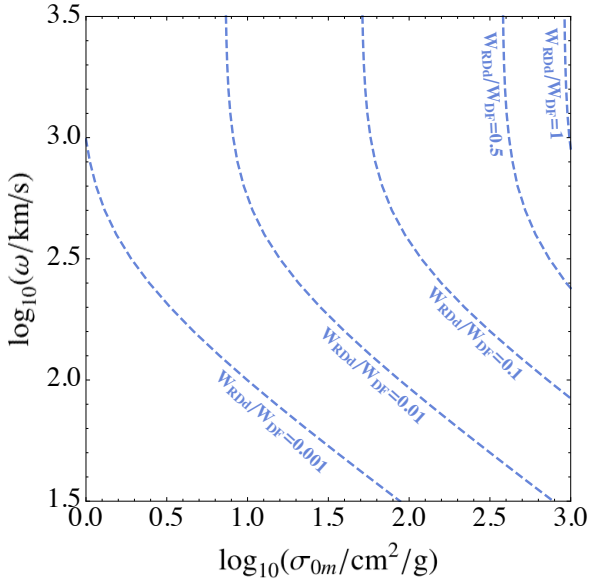


FIG. S1. Contours of the ratio of work done by ram-pressure deceleration to the work done by dynamical friction over 7 Gyr orbits for  $m_{\text{init}} = 10^{10.5} M_{\odot}$  (the result is very weakly dependent on  $m_{\text{init}}$ ) and a  $10^{12} M_{\odot}$  host. In most of the parameter space, ram-pressure deceleration plays a subdominant role in the orbital evolution of satellites.

effect is largest) the satellite's velocity is larger than the dispersions of both satellite and host, and the suppression does not enter the calculation. Figure S1 compares the role of ram-pressure deceleration to that of dynamical friction. The contours denote constant values of the ratio of work done by ram pressure to that done by dynamical friction,  $W_{\text{RPd}}/W_{\text{DF}}$ , over 7 Gyr orbits for a  $m_{\text{init}} = 10^{10.5} M_{\odot}$  satellite orbiting a  $10^{12} M_{\odot}$  host. For most of the parameter space considered, orbital decay from ram-pressure deceleration is highly subdominant to the effects of dynamical friction and only for the largest cross sections considered do the two forces produce comparable work. Although the result is plotted only for a single satellite mass in Fig. S1, the ratio  $W_{\text{RPd}}/W_{\text{DF}}$  is only mildly dependent on  $m_{\text{init}}$ . This occurs because of a cancellation between the explicit mass dependence of the dynamical friction force, and the mass dependence of the satellite's escape velocity, which enters the ram-pressure calculation.

To evaluate Eq. (S15), one must specify the initial conditions of the problem. In our case, these are: a) the virial mass of the host halo, which sets the NFW density profile through the concentration relation, and b) the initial density profile, position and velocity of the satellite. Additionally, one must specify the SIDM parameters  $\{\sigma_{0m}, \omega\}$ . The density profile of the host galaxy is assumed to follow an NFW profile in all cases. For the satellite, the initial profile depends on whether one is considering a CDM, isothermally cored SIDM, or a gravothermally collapsing scenario. For the case of CDM, one need only specify the mass of the halo, the scale radius is then set through the concentration-mass relation. For the isothermal cored SIDM scenario, after specifying the mass and calculating the scale radius, one must also specify  $t_{\text{age}}$ , which sets  $r_1$  through Eq. (S3). In this study, we always take  $t_{\text{age}} = 10$  Gyrs; this assumption is only relevant when  $r_c$  has not yet saturated  $r_s$ , which only occurs when  $\sigma_{0m} \lesssim 20 \text{ cm}^2/\text{g}$  for the range of masses considered in this study.

After having specified these values, the evolution time is divided into small time steps such that  $\Delta t \ll t_{\text{dyn}}$  and slightly larger time-steps  $\Delta T = (20\text{--}30)\Delta t$ . At each  $\Delta t$  interval,  $\Delta m_{\text{TS}}$  and  $\Delta m_{\text{RPe}}$  are calculated and  $r_{\text{trunc}}$  and  $\rho_0$  are updated accordingly. The orbit is re-evaluated for every  $\Delta T$  interval using Eq. (S15), taking the masses, density profiles, positions and velocities from the end of the previous interval as the initial conditions. The larger  $\Delta T$  interval is introduced for computational simplicity. We verify that the intervals are always small enough to have a negligible effect on the results. The final result of the calculation is the mass, density profile, position and velocity of the satellite at all times. Additionally, one can sum over  $\Delta m_{\text{TS}}$  and  $\Delta m_{\text{RPe}}$  to evaluate the total mass lost to tidal stripping and ram-pressure evaporation and perform integrals over the dynamical friction and ram-pressure deceleration to calculate the work done by these forces.

## 2. Constraints from Central Densities of Dwarf Galaxies

This Supplemental Material reviews in detail how to obtain conservative SIDM constraints using the central density of the Draco dwarf (Fig. 2, right, in the main Letter), and presents additional results for Ursa Minor, Segue 1, and Tucana 2. These constraints rely on present-day measurements of each dwarf’s central density, which are provided in Table S1. Note that for Draco and Ursa Minor, we use  $\rho_{150}$ , defined as the density at 150 pc. For Segue 1 and Tucana 2, we use the average central density,  $\bar{\rho}_{1/2}$ , within  $r_{1/2}$ , the radius within which half of the galaxy’s stellar luminosity is enclosed ( $r_{1/2} = 36$  pc for Segue 1 [58] and  $r_{1/2} = 165$  pc for Tucana 2 [59]).

The goal of this procedure is to estimate the potential of dwarf observations in constraining SIDM parameter space. Our approach is to make very conservative choices when it comes to assumptions that feed into the central density prediction. As already highlighted in the main text using Draco, the results of this exercise demonstrate the important role played by Milky Way dwarfs in constraining  $\sigma_{0m}$  and  $\omega$ . This motivates pursuing a more rigorous likelihood procedure in future work. For example, the conservative constraints presented in this work can be improved by performing a full Bayesian analysis that accounts for the unknown parameters with well-motivated priors, and appropriately stacks the contribution of each dwarf in the likelihood procedure.

There are two constraints that can be obtained using dwarf galaxies with particularly high central densities. The first (“Ram-Pressure Constraint”) is a bound that arises from the potential of ram-pressure evaporation to remove too much mass from the interior of the dwarf galaxy. The second (“Isothermal-Coring Constraint”) arises when self interactions over-core the dwarf galaxy in a region of parameter space where gravothermal collapse cannot increase the core density.

### Ram-Pressure Constraint

To evaluate the impact of ram-pressure evaporation on any given dwarf, we infer its density and concentration at infall and initialize its energy and angular momentum given present-day observations of the system and the central density profile of the Milky Way. The orbit is then evolved forwards in time. Specifically:

1. The infall mass of each satellite,  $M_{200}$ , is provided in Table S1. For the classical dwarfs, Draco and Ursa Minor, the infall masses are taken from Ref. [60]. These infall masses are inferred from abundance matching with mean star formation rates. For the ultra-faint dwarfs, Segue 1 and Tucana 2, the infall masses are taken to be  $10^9 M_\odot$ , based on the approximate upper limit of high resolution cosmological simulations with low stellar content [61]. We assume here that infall properties and star formation physics are not significantly modified by self interactions, but this remains to be tested with simulations.
2. The initial density distribution for the satellite is taken to be a fully gravothermally-collapsed profile following Eq. (S7). Importantly, gravothermal collapse in the LMFP regime cannot create arbitrarily large densities at any given radius or arbitrarily large average densities within any given radius. Specifically, below some minimal value, any additional decrease in the core size will not affect  $\rho_{150}$  or  $\bar{\rho}_{1/2}$  of the satellite. The value of  $r_c$  is chosen such that this maximal central density is achieved for each satellite. For Draco and Ursa Minor,  $r_c = 50$  pc, for Segue 1,  $r_c = 2$  pc, and for Tucana 2,  $r_c = 20$  pc. These choices correspond to the largest possible initial conditions for the central density and are therefore maximally conservative.
3. The satellite’s concentration,  $c_{200}$ , at time of infall is taken from the best-fit concentration-mass relation of Ref. [45]. We conservatively evaluate the concentration at  $z = 1$ . The star formation histories of Draco, Ursa Minor, Segue 1 and Tucana 2 suggest that their infall times may be closer to  $z \sim 2$  [62, 63]. We have verified that increasing the infall redshift decreases the initial central density and would thus strengthen the constraints.
4. The scale radius of the satellite’s halo is determined from its concentration and  $M_{200}$ , which sets the virial radius,  $r_{200}$ , through the critical density,  $\rho_{\text{crit}}$ . Additionally, the overall normalization of the density distribution,  $\rho_0$ , is obtained by requiring that the enclosed mass at  $r_{200}$  gives the virial mass.
5. The satellite’s energy and angular momentum at  $z = 0$  is estimated using its present-day velocity and position and the density profile of the Milky Way. The observations are taken from Ref. [46] for Draco, Ursa Minor, and Segue 1, and from Ref. [64] for Tucana 2.
6. The satellite’s orbit is obtained by placing it at some (arbitrary) initial position and evolving forwards in time for one pericentric passage, using the approximate values for energy and angular momentum determined in the previous step. This procedure assumes that the energy and angular momentum of the satellite at infall match its present-day values, and does not account for losses due to dynamical friction and ram-pressure deceleration. While these corrections are likely negligible for the  $\mathcal{O}(10^9) M_\odot$  halos considered here, the choice of one pericentric passage minimizes the potential impact of these approximations. Additionally, the choice of a single pericentric

Dwarf Galaxy	Central Density [ $10^7 M_\odot \text{ kpc}^{-3}$ ]	$M_{200}$ [ $M_\odot$ ]	$c_{200}(z = 1)$
Draco	16.65 [11]	$1.8 \times 10^9$ [60]	$8.84 \pm 3.36$
Ursa Minor	19.80 [11]	$2.8 \times 10^9$ [60]	$8.56 \pm 3.25$
Segue 1	92.71 [58]	$10^9$ [61]	$9.24 \pm 3.52$
Tucana 2	21.20 [59]	$10^9$ [61]	$9.24 \pm 3.52$

TABLE S1. The central densities for Draco and Ursa Minor correspond to the  $1\sigma$  lower limit on the measured  $\rho_{150}$ , and for Segue 1 and Tucana 2 correspond to the  $1\sigma$  lower limit on the measured  $\bar{\rho}_{1/2}$  (note that in the main text the Draco bound corresponds to the  $2\sigma$  lower limit). We use the concentration-mass relation from Ref. [45].  $M_{200}$  is the infall mass at  $z = 1$ .

passage avoids issues related to gravothermal collapse potentially occurring between passages. The constraints would significantly strengthen the more pericentric passages are included, since more mass is removed from the satellite during each of these.

7. After evolving for a single orbit, the central density (either  $\rho_{150}$  or  $\bar{\rho}_{1/2}$ ) is found and compared to the  $2\sigma$  lower limit from observations for results shown in Fig. 2 and to the  $1\sigma$  lower limit for results shown in Fig. S2. If the predicted value is larger than the observational lower limit, then the point in the  $\{\sigma_{0m}, \omega\}$  parameter space is excluded.
8. The calculation is performed for two different Milky Way masses,  $1 \times 10^{12}$  and  $1.6 \times 10^{12} M_\odot$ , which correspond to the lower and upper  $1\sigma$  limits quoted in Ref. [47].

### Isothermal-Coring Constraint

To evaluate the impact of isothermal coring on any given dwarf, we determine its density distribution at present day while requiring that gravothermal collapse has not yet occurred. Specifically:

1. The density profile of the satellite is modeled by Eq. (S2). The halo is assumed to relax for  $t_{\text{age}} = 10$  Gyrs, which sets the value of  $r_1$  following Eq. (S3).
2. The concentration of the satellite is taken from the  $2\sigma$  upper limit of the concentration-mass relation from Ref. [45] at  $z = 1$ —see Table S1.
3. Determining the central density of the profile requires knowing its current mass,  $m_{\text{sat}}$  (which determines  $r_s$ ). Because the current mass of the satellite is not well constrained, we evaluate the central density (either  $\rho_{150}$  or  $\bar{\rho}_{1/2}$ ) for a grid of masses in the range  $m_{\text{sat}} \in [10^7 M_\odot, M_{200}]$  and, for every point in the  $\{\sigma_{0m}, \omega\}$  parameter space, choose the value of  $m_{\text{sat}}$  for which the central density is largest. These correspond to conservative choices for the satellite mass. The resulting value of the central density is then compared to the  $2\sigma$  lower limit from observations for results shown in Fig. 2 and to the  $1\sigma$  lower limit for results shown in Fig. S2. If the predicted value is larger than the observational lower limit, then the point in the  $\{\sigma_{0m}, \omega\}$  parameter space is excluded. This sets the left-most contour of the isothermal-coring bound. An important point is that as the cross section increases, the core size increases only until it reaches its maximal value at around  $r_c = r_s$ . For larger cross sections, the central density no longer decreases but rather remains constant. Therefore, much of the excluded parameter space is constrained at the same confidence level.
4. The right-most contour of the isothermal-coring bound is set by the requirement that gravothermal collapse be inactive. Specifically, we estimate the gravothermal-collapse timescale,  $t_{\text{GC}}$ , using [28]

$$t_{\text{GC}} \approx \frac{290}{\langle \sigma_m v \rangle \rho_{\text{core}}} , \quad (\text{S18})$$

and require that  $t_{\text{GC}} > 20$  Gyrs. This choice accounts for potential shortening of  $t_{\text{GC}}$  through the effects of tidal stripping, based on the results of Ref. [32]. For the velocity average, the dispersion is taken to be  $\sigma_r = 1.1 \times v_{\text{max}} / \sqrt{3}$ , where  $v_{\text{max}}$  is the maximal circular velocity of the NFW profile at radius  $r_{\text{max}} > r_c$ . This

may be derived from the maximum dispersion for a NFW halo  $\text{Max}(v_{\text{rms}})$  using the Taylor-Navarro [65] phase-space density  $Q(r) = \rho(r)/v_{\text{rms}}(r)^3 = 0.3/(Gv_{\text{max}}r_{\text{max}}^2(r/r_s)^{-\eta})$  with  $\eta \simeq 2$  [66]. The median radial dispersion to  $v_{\text{max}}$  ratio plotted in Ref. [67] provides similar values (but about 10% higher).

In the time scale defined above,  $\rho_{\text{core}}$  is taken to be the central density of the isothermal cored SIDM profile, which should be interpreted as the minimum core density in the evolution of the halo. Note that since  $v \propto v_{\text{max}}$  and  $\rho_{\text{core}} \propto \rho_0$ , this time scale has the same dependence on the initial profile as that in Ref. [32]. However, the time scale used here is roughly a factor of two larger than that in Ref. [32], which can be traced back to the choice of the LMF conductive normalization used to get a fit to halo profiles for moderate cross sections  $\lesssim 10 \text{ cm}^2/\text{g}$ . The formula used here for  $t_{\text{GC}}$  is more consistent with the evolution of the core density for large cross sections [28, 31]. We evaluate  $t_{\text{GC}}$  for a grid of masses in the range  $m_{\text{sat}} \in [10^7 M_{\odot}, M_{200}]$  for every point in the  $\{\sigma_{0m}, \omega\}$  parameter space. The constraints do not extend to points in parameter space where  $t_{\text{GC}} > 20$  Gyrs for any mass within this range.

The final results for the classical dwarfs Draco and Ursa Minor, as well as the ultra-faint dwarfs Segue 1 and Tucana 2, are provided in Fig. S2. For these results, we have used the  $1\sigma$  lower limits on measurements of  $\rho_{150}$  for Draco and Ursa Minor, and of  $\bar{\rho}_{1/2}$  for Segue 1 and Tucana 2. The choice of  $1\sigma$ , as opposed to the  $2\sigma$  lower limit used for the Draco bound in the main text, illustrates the strong sensitivity of the isothermal coring bound to this choice. This sensitivity is due to the fact that central densities of an isothermal cored profile change slowly as  $\sigma_{0m}$  is varied. The ram-pressure bounds are much less sensitive to small variations in the measurement of  $\rho_{150}$  or  $\bar{\rho}_{1/2}$ .

The additional systems complement the result for Draco in a number of ways. Firstly, Draco's orbit has been shown to potentially be affected by the Large Magellanic Cloud (LMC) [46]. If this is the case, then a full analysis should include the effects of Draco's interactions with the halo of the LMC and also account for the three-body orbit, both of which are beyond the scope of this work. However, the same study shows that Ursa Minor, which has a similar central density to Draco, is far less affected by the LMC. Specifically, the pericenter of Ursa Minor's orbit is expected to change far less when accounting for the multi-body orbit of the dwarf, LMC and the Milky Way. Second, Segue 1 and Tucana 2 are more DM dominated than either Draco or Ursa Minor, and thus have a different set of observational systematics. Finally, it is possible that the large central densities of the objects considered in this study could be the result of anomalously high concentrations, beyond even the  $2\sigma$  upper limit values used for results where gravothermal collapse does not occur ( $2\sigma$  was chosen specifically because we consider some of the densest known satellites of the Milky Way). If this is the case, the constraints would weaken. However, the combination of all four analyses illustrates the point that a future study of an ensemble of dwarfs will provide a robust constraint on the SIDM parameter space.

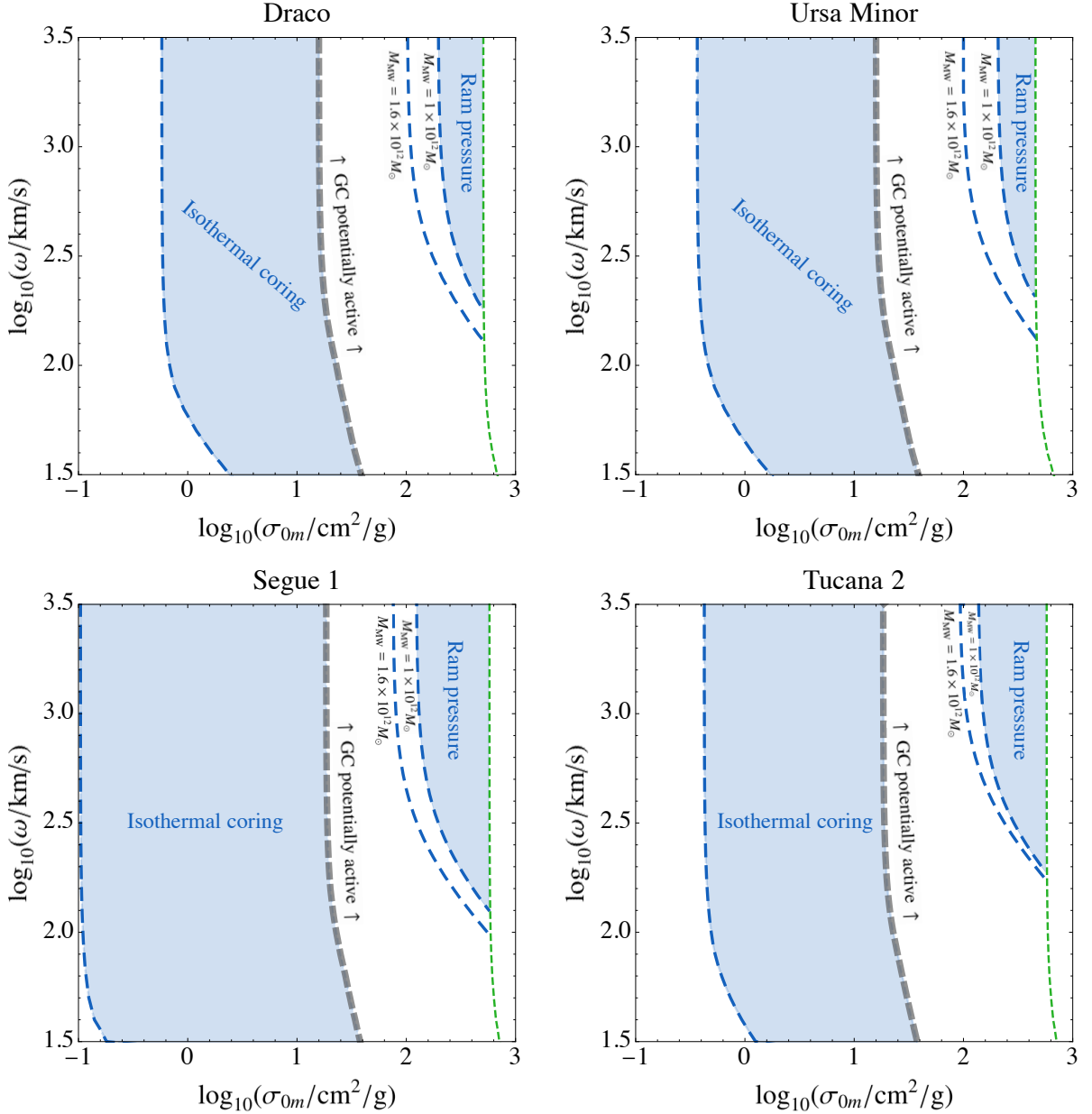


FIG. S2. Constraints similar to those of Fig. 2 (right) for three additional systems: the classical dwarf Ursa Minor and the ultra-faint dwarfs Segue 1 and Tucana 2. For completeness, the Draco bound is shown here as well. For these constraints, the  $1\sigma$  lower limit on measurements of  $\rho_{150}$  or  $\bar{\rho}_{1/2}$  are used. Note that the Draco bound shown here takes the  $1\sigma$  lower limit on the measured  $\rho_{150}$ , whereas that in Fig. 2 (right) takes the  $2\sigma$  lower limit.